Accepted Manuscript

Thermal signature of ion intercalation and surface redox reactions mechanisms in model pseudocapacitive electrodes

Obaidallah Munteshari, Jonathan Lau, Ampol Likitchatchawankun, Bing-Ang Mei, Christopher S. Choi, Danielle Butts, Bruce Dunn, Laurent Pilon

PII: S0013-4686(19)30617-6

DOI: https://doi.org/10.1016/j.electacta.2019.03.185

Reference: EA 33901

To appear in: *Electrochimica Acta*

Received Date: 12 February 2019

Revised Date: 25 March 2019

Accepted Date: 26 March 2019

Please cite this article as: O. Munteshari, J. Lau, A. Likitchatchawankun, B.-A. Mei, C.S. Choi, D. Butts, B. Dunn, L. Pilon, Thermal signature of ion intercalation and surface redox reactions mechanisms in model pseudocapacitive electrodes, *Electrochimica Acta* (2019), doi: https://doi.org/10.1016/j.electacta.2019.03.185.

Thermal signature of ion intercalation and surface redox reactions mechanisms in model pseudocapacitive electrodes

Obaidallah Munteshari[a,b], Jonathan Lau[c], Ampol Likitchatchawankun[a], Bing-Ang Mei[a,d], Christopher S. Choi[c], Danielle Butts[c], Bruce Dunn[c], and Laurent Pilon[a,+]

[a]Mechanical and Aerospace Engineering Department, Henry Samueli School of Engineering and Applied Science, University of California, Los Angeles, CA 90095, USA

[b]Mechanical Engineering Department, King Fahd University of Petroleum and Minerals (KFUPM), Dhahran 31261, Saudi Arabia

[c]Materials Science and Engineering Department, Henry Samueli School of Engineering and Applied Science, University of California, Los Angeles, CA 90095, USA

[d]School of Mechanical Engineering, Beijing Institute of Technology, Beijing 100081, China

[+]Corresponding Author: Phone: +1 (310)-206-5598, Fax: +1 (310)-206-2302

E-mail: pilon@seas.ucla.edu

March 27, 2019

Abstract

This study aims to investigate the thermal signature associated with the charge storage mechanisms in hybrid supercapacitors using *in operando* calorimetry under constant current cycling. The hybrid supercapacitors consisted of highly porous pseudocapacitive electrode and activated carbon (AC) electrode with either organic or aqueous electrolytes. Pseudocapacitive electrodes made of either molybdenum dioxide on reduced graphene oxide (MoO_2-rGO) or manganese dioxide on graphene (MnO_2-G) were synthesized to investigate heat generation associated with reversible redox reactions involving ion intercalation or fast surface redox reactions, respectively. Here, MoO_2-rGO served as the negative electrode against activated carbon electrode in 1 M $LiClO_4$ in EC:DMC. In addition, electrolyte consisting of 1 M $TBABF_4$ in EC:DMC was also used as a reference to suppress redox reactions and intercalation due to its large ionic size. On the other hand, mesoporous MnO_2-G electrode served as the positive electrode also against activated carbon electrode but in 0.5 M aqueous Na_2SO_4. First, a data analysis procedure was developed to distinguish between irreversible and reversible heat generation rates and to isolate Joule heating from the measured instantaneous heat generation rate at each electrode. In the AC electrodes, the irreversible heat generation rate was due to resistive losses (i.e., Joule heating) while the reversible heat generation was due to ion adsorption/desorption at the electrolyte/electrode interface. By contrast, irreversible heat generation rate in the pseudocapacitive electrodes exceeded Joule heating. This was attributed to irreversible heat generation associated with redox reactions, polarization heating, and hysteresis in EDL formation and dissolution. Finally, MoO_2-rGO negative electrode in $LiClO_4$ featured endothermic reversible heat generation during charging due to Li^+ intercalation. Similarly, MnO_2-G positive electrode in Na_2SO_4 featured endothermic heat generation during charging due to non-spontaneous surface redox reactions.

Keywords: heat generation; thermal management; charging mechanism; molybdenum oxide; manganese oxide

NOMENCLATURE

A	Footprint area of the heat flux sensor, cm^2
C	Charge capacity, mAh
C_g	Gravimetric charge capacity, Ah/g
H	Stern layer thickness, nm
I	Current, mA
I_g	Gravimetric current, A/g
m	Mass of redox active material loaded into the pseudocapacitive electrode, mg
n	Cycle number
q''	Heat flux, mW/cm^2
$\dot{Q}$	Heat generation rate, mW
$\bar{\dot{Q}}$	Time-averaged heat generation rate, mW
R_s	Internal resistance for entire EDLC device, Ω
S_i	Heat flux sensor sensitivity at electrode "i", $\mu V/(mW/cm^2)$
S	Entropy of the system, J/K
t	Time, s
t_c^-	Time immediately after the beginning of the discharging step, s
t_c^+	Time at the end of the charging step, s
ΔV	Voltage difference generated in the heat flux sensor, μV

Greek symbols

ϵ_0	Vacuum permittivity, F/m
ϵ_r	Dielectric constant of the electrolyte
η	Overpotential, V
ν	Scan rate, mV/s
ψ_s	Potential across an EDLC cell, V

Superscripts and subscripts

AC	Refers to activated carbon electrode
c	Refers to charging step
cd	Refers to charging-discharging cycle
i	Refers to electrode i = AC, MnO_2-G, or MoO_2-rGO
irr	Refers to irreversible processes
J	Refers to Joule heating
max	Refers to maximum value
min	Refers to minimum value
$other$	Refers to heating associated with phenomena other than Joule heating
P	Refers to pseudocapacitive electrode
T	Refers to entire cell
rev	Refers to reversible process

1 Introduction

Electrochemical capacitors (ECs) differ from batteries by their high power density, long cycle life, and high cycle efficiency [1]. Depending on their charging mechanism, ECs can be classified as electric double layer capacitors (EDLCs) or hybrid supercapacitors [1, 2]. EDLCs are typically made of carbon-based electrodes and store charges physically via electric double layer formation as ions accumulate at the electrode/electrolyte interface [1, 2]. On the other hand, hybrid supercapacitors typically consist of a positive or negative pseudocapacitive electrode and a carbon-based counter electrode [3]. The pseudocapacitive electrode stores charges chemically via reduction/oxidation (redox) reactions at/or near the electrode surface in addition to EDL formation [2, 4]. These redox reactions may be accompanied by ion intercalation/deintercalation. In batteries, redox reactions are typically associated with phase transformation in the electrode material responsible for degradation and relatively shorter lifetime [5]. By contrast, phase transformation is absent in pseudocapacitive electrodes leading to fast and highly reversible charging/discharging [4].

Transition metal oxides (e.g., Nb_2O_5, MnO_2, MoO_2, MoS_2) have been considered as pseudocapacitive electrode materials due to their high theoretical capacity, chemical stability, and high redox reaction reversibility [6]. Two charging mechanisms have been proposed to explain the electrochemical behavior of metal oxide (M_xO_y) electrodes namely by (1) redox reactions with ions intercalation/deintercalation (as in Nb_2O_5) according to [4],

$$M_xO_y + zA^+ + ze^- \underset{\text{discharging}}{\overset{\text{charging}}{\rightleftharpoons}} A_zM_xO_{y-z} \tag{1}$$

and (2) by fast surface redox reactions (as in $RuO_2.nH_2O$) [7],

$$[M_xO_y]_{\text{surface}} + zA^+ + ze^- \underset{\text{charging}}{\overset{\text{discharging}}{\rightleftharpoons}} \left[(A_z^+)(M_xO_{y-z}^-)\right]_{\text{surface}} \tag{2}$$

Here, A^+ refers to alkali metal cations such as Li^+, Na^+, and K^+. The charging mechanism of pseudocapacitive electrode is typically identified by its electrochemical signature. Ion intercalation/deintercalation charging mechanism typically features larger current and distinct redox peaks in CV curves and non-linear potential evolution and fast charging under

galvanostatic cycling [4]. On the other hand, CV curves associated with fast surface redox reactions are nearly rectangular while their potential varies linearly with time under constant current cycling similar to those associated with electrical double layer formation [4].

The present study aims to investigate the time-dependent heat generation associated with EDL formation/dissolution, redox reactions with intercalation/deintercalation, and fast surface redox reactions during charging and discharging of hybrid supercapacitors. Indeed, the thermal signature of these phenomena can help identify and provide unique insights into the charging mechanisms. To do so, time-dependent heat generation rates at the electrodes of hybrid supercapacitors were investigated by *in operando* calorimetry under galvanostatic cycling. The devices consisted of model pseudocapacitive electrodes made of molybdenum dioxide (MoO_2) or manganese dioxide (MnO_2) and activated carbon (AC) counter electrode.

2 Background

Transition metal oxides MoO_2 and MnO_2 have previously been evaluated as pseudocapacitive materials for high-rate applications [8, 9]. First, MoO_2 stores charge through intercalation pseudocapacitance and is typically used as a negative electrode in hybrid supercapacitors due to the relatively low potential range of redox reactions versus Li/Li^+ [8]. Conversely, MnO_2 stores charge through fast surface redox reactions and has previously been used as a positive electrode in hybrid supercapacitors [7]. Therefore, MoO_2 and MnO_2 constitute ideal model materials to investigate the thermal signature of the different charging mechanisms in pseudocapacitive electrodes.

2.1 Molybdenum dioxide MoO_2

MoO_2 has attracted considerable attention as a promising negative electrode materials in Li-ion batteries thanks to its low electrical resistivity and high energy density [10–12]. However, bulk MoO_2 material suffers from poor redox reversibility, slow Li^+ diffusion, and large volume expansion upon lithiation leading to poor electrochemical performance [8]. Thus, MoO_2

nanoparticles have been synthesized to improve the rate and reversibility of Li^+ intercalation/deintercalation process [8, 12]. For example, Kim et al. [8] found that the use of MoO_2 nanoparticles suppresses the phase transformation and improves pseudocapacitive intercalation/deintercalation. Moreover, synthesizing MoO_2 nanoparticles on reduced graphene oxide (rGO) was found to improve the electrode conductivity and capacity and provide mechanical support to the electrode structure [8].

2.2 Manganese dioxide MnO_2

MnO_2 has been widely used as a pseudocapacitive electrode thanks to its low toxicity, high theoretical capacity, and low cost compare to that of hydrous ruthenium oxide ($RuO_2 \cdot xH_2O$) [7]. Mesoporous MnO_2 usually serves as a positive electrode in aqueous electrolytes due to its relatively narrow electrochemical potential window [13]. The lower cut-off potential (~ -0.1 V vs. Ag/AgCl) is limited by the manganese dissociation in the electrolyte while the upper cut-off potential ($\sim$ 0.9 V vs. Ag/AgCl) is limited by the irreversible oxygen evolution reaction [13].

Ragupathy et al. [14] suggested that fast surface redox reactions occur mostly in amorphous MnO_2 while intercalation/deintercalation takes place in crystalline MnO_2 compounds. In addition, Toupin et al. [7] investigated the charging mechanism of thin (< 5 μm) and thick (~ 100 μm) amorphous MnO_2 electrodes in 0.1 M Na_2SO_4 aqueous electrolyte using *ex situ* X-ray photoelectron spectroscopy (XPS). The gravimetric capacitance of thin MnO_2 electrodes approached the theoretical maximum for redox reactions involving one electron per manganese atom and was much larger than that of thick MnO_2 electrodes [7]. In fact, the bulk of thick MnO_2 electrode did not show any variation in its oxidation state upon cycling [7]. Therefore, the authors concluded that redox reactions were only taking place in a thin surface layer of MnO_2 electrode suggesting that charging occurred by fast surface redox reactions [7]. By contrast, Iamprasertkun et al. [15] reported that protons (H^+) intercalate/deintercalate into MnO_2 nanosheet electrodes in aqueous electrolyte with pH $<$ 2.03 while Na^+ intercalation/deintercalation dominate for 2.03 $<$ pH $<$ 4.02. However, at

pH > 5.3, the specific capacitance of MnO_2 nanosheet electrodes significantly decreases [15]. The authors attributed this decrease to the limited adsorption/desorption of solvated anions since the MnO_2 is negatively charged at pH > 5.3 [15]. Finally, synthesizing MnO_2 on graphene scaffold increases the surface area of the composite, maximizes surface redox sites, and improves the electrical conductivity of the electrode [9].

2.3 Heat generation in pseudocapacitive electrodes

2.3.1 Experiments

Dandeville et al. [16] developed an isothermal calorimeter measuring the time-dependent temperature in electrochemical capacitors under galvanostatic cycling and retrieved the heat generation rate in the entire device by deconvolution analysis. The authors examined (i) an EDLC device consisting of two identical 250 μm thick AC electrodes and (ii) a hybrid supercapacitor consisting of a 250 μm thick positive electrode made of mesoporous MnO_2 and a negative electrode made of AC. The electrolyte used in both devices was 0.5 M aqueous K_2SO_4. The calorimeter measured the time-dependent heat generation rate in the entire cell. Then, the data analysis assumed that (i) the heat generation rate $\dot{Q}_T^{\mathrm{EDLC}}(t)$ in the EDLC device was evenly divided between the two AC electrodes as $\dot{Q}_{\mathrm{AC}}^{\mathrm{EDLC}}(t) = \dot{Q}_T^{\mathrm{EDLC}}(t)/2$ and (ii) the heat generation rate $\dot{Q}_{\mathrm{AC}}^{\mathrm{H}}(t)$ in the AC of the hybrid supercapacitor was the same as that in the EDLC, i.e., $\dot{Q}_{\mathrm{AC}}^{\mathrm{H}}(t) = \dot{Q}_{\mathrm{AC}}^{\mathrm{EDLC}}(t)$. Then, the instantaneous heat generation rate in the MnO_2 electrode $\dot{Q}_{\mathrm{MnO_2}}^{\mathrm{H}}(t)$ was expressed as a function of the total heat generation rate $\dot{Q}_T^{\mathrm{H}}$ in the hybrid supercapacitor according to [16],

$$\dot{Q}_{\mathrm{MnO_2}}^{\mathrm{H}} = \dot{Q}_T^{\mathrm{H}} - \dot{Q}_{\mathrm{AC}}^{\mathrm{H}} = \dot{Q}_T^{\mathrm{H}} - \frac{\dot{Q}_T^{\mathrm{EDLC}}}{2} \tag{3}$$

The results indicated that (i) the irreversible heat generation rate in the electrodes of the hybrid supercapacitor was only due to Joule heating and (ii) the reversible heat generation rate in the AC electrode was exothermic during charging and endothermic during discharging and (iii) the reversible heat generation rate in the MnO_2 positive electrode was endothermic during charging and exothermic during discharging due to redox reactions [16].

Moreover, we have recently investigated heat generation rate in EDLC devices using *in operando* calorimeter capable of measuring heat generation at each electrode individually [17, 18]. First, the irreversible heat generation rate at each electrode and in the device was due to Joule heating [17–19]. Second, although the positive and negative electrodes of the EDLC devices were identical and made of AC, our measurements established that reversible heat generation rate may be different in the two electrodes for both organic and aqueous electrolytes [17]. In addition, the time-averaged reversible heat generation at the positive electrode was linearly proportional to the current while it was independent of current and nearly zero at the negative electrode [17]. This asymmetry in the heat generation rate was attributed to asymmetry in the charging mechanism due to interactions between anionic functional groups of carboxymethyl cellulose (CMC) used as a binder in the electrode and the cations at the negative electrode [18].

2.3.2 Numerical simulations

D'Entremont and Pilon [20] developed a thermal model to estimate local time-dependent heat generation rate in hybrid supercapacitors. The authors simulated an electrochemical cell consisting of a pseudocapacitive positive electrode and a carbon-based negative electrode with 1 M lithium perchlorate ($LiClO_4$) in propylene carbonate (PC) as the electrolyte. The authors assumed that pseudocapacitive electrode reacted reversibly with Li^+ within the Stern layer near its surface while intercalation of Li^+ in the electrode was modeled as a diffusion process [20]. Two regimes were identified in the charging step namely (i) a faradaic regime occurring at low current densities and controlled by redox reactions and (ii) a capacitive regime occurring at high current densities and dominated by EDL formation [20]. Irreversible heat generation at the carbon-based electrode was due to Joule heating [20]. At the pseudocapacitive electrode, the irreversible heat generation was also due to Joule heating in the capacitive regime [20]. However, in the faradaic regime, the total irreversible heat generation rate at the pseudocapacitive electrode was not only due to Joule heating but also to polarization heating (termed as irreversible faradaic heat generation) and hysteretic EDL

formation [20]. Polarization heating is defined as the product of overpotential η and current I [20, 21]. On the other hand, redox reactions at the pseudocapacitive electrode surface interfered with EDL formation resulting in hysteresis in the ion concentrations upon charging and discharging [20]. This, in turn, led to the time-averaged heat generation associated with EDL formation to be strictly positive (i.e., irreversible) [20]. Note that, this deviation from Joule heating was not observed experimentally in Ref. [16] for MnO_2/AC hybrid supercapacitor possibly due to the use of relatively thick and thus resistive electrodes and/or to the invalid assumptions made in estimating heat generation at individual electrodes. Finally, in the faradaic regime, the numerically predicted reversible heat generation rate at the pseudocapacitive electrode was endothermic during charging by deintercalation and exothermic during discharging by intercalation [20], as observed experimentally [16].

The present study aims to investigate the thermal behavior associated with EDL formation/dissolution, redox reactions with intercalation/deintercalation, and fast surface redox reactions in pseudocapacitive electrodes of hybrid supercapacitors. Electrode made of MoO_2 nanoparticles on reduced graphene oxide (rGO) and MnO_2 nanoparticles on graphene (G) pseudocapacitive electrodes were synthesized. *In operando* heat generation measurements could discriminate between these charging mechanisms based on the hypothesis that they have distinct thermal signatures.

3 Materials and methods

3.1 AC/MoO_2-rGO hybrid supercapacitor

First, AC slurry was prepared by ball-milling YP-50F activated carbon (Kuraray), Super P (Alfa Aesar), and multiwall carbon nanotubes (mwCNT, Sigma Aldrich) as conducting additives with weight ratio of 88:6:6. The carbon mixture was then mixed in a slurry with styrene-butadiene rubber (SBR, MTI Corporation) as a binder and carboxymethylcellulose (CMC, DOW Chemical) as a binder and thickening agent with weight ratio of 90:6:4.

Second, MoO_2 nanoparticles were synthesized on rGO scaffold according to a previously

reported hydrothermal synthesis with minor modification [8]. In brief, 270 mg of $MoCl_5$ (Alfa Aesar) was dissolved in a mixture of 5 mL ethanol, 5 mL DI water, and 10 mL of graphene oxide suspension in water (5 g/L prepared from the modified Hummers method [22, 23]) in a 45 mL Teflon liner. Heat treatment of the suspension was carried out in an autoclave at 180°C for 6 hours. The MoO_2-rGO nanoparticles were washed and centrifuged twice with ethanol before drying in an oven at 100°C for 12 hours. Here, MoO_2 represented 88 wt.% of the MoO_2-rGO nanoparticles composite. Then, MoO_2-rGO slurries were prepared by mixing a slurry of MoO_2-rGO, Super P (Alfa Aesar), mwCNT, and PVDF binder in N-methyl pyrrolidinone (NMP) with weight ratio of 70:10:10:10. Thus, the mass of MoO_2 in MoO_2-rGO electrode was 0.616 mg.

Third, the AC and MoO_2-rGO slurries were drop-cast onto 1×1 cm^2 carbon-coated aluminum current collectors (MTI) with mass loading of 3.7 and 1 mg/cm^2, respectively. The AC electrode was mass overloaded with respect to MoO_2-rGO electrode in order to (i) ensure that the MoO_2-rGO electrode fully charged and discharged during cycling and to (ii) avoid excessive electrolyte degradation at high potentials at the AC electrode [24]. The electrodes were dried under vacuum at 120°C for 24 hours before being placed in a glove box under argon atmosphere. Prior to assembly of the hybrid supercapacitor, AC and MoO_2-rGO electrodes were pre-cycled in a three-electrode flask with lithium metal counter and reference electrodes. In assembling the two-electrode device, a 350 μm glass fiber (GF85 filter, Advantec MFS Inc.) was used as a separator and as thermal insulator between the electrodes. In order to avoid exposure to ambient atmosphere, the hybrid supercapacitor was assembled, installed, and sealed in the isothermal calorimeter inside the glove box. For both the three-electrode measurements and the full-cell AC/MoO_2-rGO calorimetric measurements, the electrolyte was 1 M $LiClO_4$ in ethylene carbonate:dimethyl carbonate (EC:DMC, Sigma-Aldrich) with 1:1 volume ratio.

Moreover, in order to discriminate between the contribution of EDL formation and Li^+ ions intercalation/deintercalation into MoO_2-rGO electrodes, a hybrid supercapacitor (Device 2) identical to Device 1 was also tested but with 1 M tetrabutylammonium tetraflu-

oroborate ($TBABF_4$) in EC:DMC (1:1 weight ratio) as the electrolyte for the same potential window. Indeed, the size of solvated TBA^+ ($\sim$ 1.16 nm [25]) is much larger than that of Li^+ ($\sim$ 0.41 nm [26]) and larger than the van der Waals gap of MoO_2 making intercalation of TBA^+ into MoO_2 limited so that mainly EDL formation contributed to charging [27].

3.2 MnO_2-G/AC hybrid supercapacitor

First, AC slurry was prepared by mixing YP-50F activated carbon (Kuraray), Super P (Alfa Aesar) as a conducting agent, and PVDF as a binder dissolved in N-methyl pyrrolidinone (NMP) with weight ratio of 70:20:10 [28].

Second, MnO_2 nanoparticles were synthesized on graphene (G) using a microwave synthesis adapted from a previously reported procedure [9]. In a typical synthesis, 90 mg of KS6 synthetic graphite (Imerys) was added to 50 mL of deionized (DI) water and sonicated until a stable suspension was obtained ($\sim$ 1 h). Then, 450 mg of $KMnO_4$ (Sigma Aldrich) was added to the graphene suspension and stirred for 5 min and sonicated for another 30 min. The suspension was then heated to 185°C for 1 hour using a microwave oven (Discover SP-Microwave Synthesizer, CEM). The MnO_2-G composite was washed and centrifuged with DI water five times before being dried in a 100°C oven overnight. Here, MnO_2 represented 85 wt.% of the MnO_2-G composite. The slurry of MnO_2-G electrode was prepared by mixing the MnO_2-G composite material, Super P, and PVDF in NMP with weight ratio of 70:20:10. Therefore, the mass of MnO_2 in MnO_2-G electrode was 0.714 mg.

AC and MnO_2-G slurries were drop-cast onto 1×1 cm^2 nickel foil (Alfa Aesar) current collectors with a mass loading of 2.3 mg/cm^2 and 1.2 mg/cm^2, respectively. Here also, the AC electrode was mass-overloaded for the same reasons as those previously mentioned. The electrodes were dried in ambient air overnight and then in an oven at 120°C for at least 2 hours prior to electrochemical testing. Prior to full-cell assembly of Device 3, individual AC and MnO_2-G electrodes were pre-cycled in a three-electrode flask with AC counter electrode and Ag/AgCl reference electrode. Here, 0.5 M Na_2SO_4 in DI water (pH $\sim$ 7 as measured by pH probe) was used as the electrolyte for both three-electrode and full-cell MnO_2-G/AC

measurements. Similar to Devices 1 and 2, Device 3 used a 350 μm glass fiber (GF85 filter, Advantec MFS Inc.) as a separator and as thermal insulator between the electrodes.

Table 1 summarizes the components of the three devices considered in this study along with the potential window ($\psi_{s,min}$, $\psi_{s,max}$). The potential window of Devices 1 and 2 ranged from 0.5 to 2.5 V. On the other hand, the potential window of Device 3 ranged from 0.4 to 1.4 V due to limits imposed by the electrolytes.

Table 1: Components and potential window for the three hybrid supercapacitors studied.

Device	**Positive electrode**	**Negative electrode**	**Electrolyte**		$\psi_{s,min}$	$\psi_{s,max}$
No.	**(Mass loading)**	**(Mass loading)**	**Salt**	**Solvent**	**(V)**	**(V)**
1	AC (3.7 mg/cm^2)	MoO_2-rGO (1 mg/cm^2)	1 M $LiClO_4$	EC:DMC	0.5	2.5
2	AC (3.7 mg/cm^2)	MoO_2-rGO (1 mg/cm^2)	1 M $TBABF_4$	EC:DMC	0.5	2.5
3	MnO_2-G (1.2 mg/cm^2)	AC (2.3 mg/cm^2)	0.5 M Na_2SO_4	DI water	0.4	1.4

Finally, nitrogen adsorption/desorption isotherms were measured at -196 °C on an accelerated surface area and porosity analyzer (ASAP2010, Micromeritics Instruments Corp.). Specific surface area was calculated using the Brunauer-Emmett-Teller method (BET) based on nitrogen adsorption data in the relative pressure range 0.05-0.3 and assuming the cross-sectional area of a nitrogen molecule to be 0.162 nm^2 [29, 30]. The specific surface area of MoO_2-rGO and MnO_2-G composites were found to be 58 and 56 m^2/g, respectively.

3.3 *In operando* calorimeter

We recently reported on the design, fabrication, and demonstration of an *in operando* calorimeter apparatus to measure, during operation, the instantaneous heat generation rate at individual electrode of electrochemical capacitors [17]. Details of the experimental setup, validation, and data analysis have been reported and need not be repeated [17]. In brief, the *in operando* calorimeter used thermoelectric heat flux sensors in thermal contact with each electrode to measure the time-dependent heat generation rate therein [17]. The two

electrodes were thermally insulated from one another by a glass fiber separator.

Based on the thermal analysis of a single electrode described in supplementary material of Ref. [17], the instantaneous heat generation rate $\dot{Q}_i(t)$ (in mW) at electrode "i" can be obtained from the heat flux q_i'' measured at the heat flux sensor/electrode interface according to,

$$\dot{Q}_i(t) = q_i'' A_i = \frac{\Delta V_i(t)}{S_i} A_i \qquad \text{with } i = \text{ AC, } MoO_2\text{-rGO, or } MnO_2\text{-G} \tag{4}$$

where $\Delta V_i(t)$ is the voltage difference (in μV) measured from the heat flux sensor while S_i and A_i are the sensor temperature-dependent sensitivity (in $\mu V/(mW/cm^2)$) and footprint area (in cm^2), respectively. Both S_i and A_i were provided by the manufacturer [31]. The subscript "i" refers to either the activated carbon "AC", pseudocapacitive "MoO_2-rGO", or "MnO_2-G" electrodes. The total heat generation rate in the entire cell denoted by subscript "T" can be expressed as $\dot{Q}_T(t) = \dot{Q}_{\text{AC}}(t) + \dot{Q}_{\text{MoO}_2\text{-rGO}}(t)$ for Devices 1 and 2 or $\dot{Q}_T(t) = \dot{Q}_{\text{AC}}(t) + \dot{Q}_{\text{MnO}_2\text{-G}}(t)$ for Device 3.

3.4 Experimental procedure

First, cyclic voltammetry (CV) was used to determine charge capacity C (in mAh) of individual electrodes and of the full cell evaluated by integrating the area enclosed by the CV curve plotting the measured current I versus the imposed potential $\psi_s(t)$ for a given scan rate ν according to [32],

$$C(\nu) = \oint \frac{I(\psi_s)}{2\nu} \mathrm{d}\psi_s. \tag{5}$$

Moreover, the gravimetric charge capacity C_g (in Ah/g) and gravimetric current I_g (in A/g) can be expressed, respectively, as,

$$C_g(\nu) = \frac{C(\nu)}{m} \quad \text{and} \quad I_g = \frac{I}{m} \tag{6}$$

where m is the mass of the redox active material (i.e., MoO_2 or MnO_2) in the pseudocapacitive electrode.

In addition, the internal resistance R_s (or DC resistance) (in Ω) of the device was determined from the IR drop observed at the charging/discharging transition of the cell

potential $\psi_s(t)$ near t_c under galvanostatic cycling with constant current I according to [33–36],

$$R_s(I) = \frac{\psi_s(t_c^+) - \psi_s(t_c^-)}{2I}. \quad (7)$$

Here, $\psi_s(t_c^+)$ and $\psi_s(t_c^-)$ are the potentials across the cell at the end of the charging step and immediately after the beginning of the discharging step, respectively. Here, the IR drop $[\psi_s(t_c^+) - \psi_s(t_c^-)]$ was obtained by estimating the cell potential $\psi_s(t_c^-)$ 10 ms after the beginning of the discharging step at t_c^+ (i.e., $t_c^- - t_c^+ = 10$ ms), as suggested by Zhao et al. [34].

Finally, the time-dependent heat generation rate $\dot{Q}_i(t)$ at each electrode was measured under galvanostatic cycling for imposed constant current I ranging from 2 to 6 mA corresponding to gravimetric current I_g between 3.2 and 9.7 A/g for Devices 1 and 2 and between 2.8 and 8.4 A/g for Device 3. Note that, the heat generation measurements at low current (i.e., $I \leq 1$ mA) fell below the detection level (< 0.01 mW) of the calorimeter introducing a significant error in the measurements.

4 Results and discussion

4.1 Individual electrode characterization

Figure 1 shows the potential evolution versus capacity from three-electrode measurements for (a) AC and MoO_2-rGO electrodes in 1 M $LiClO_4$ in 1:1 EC:DMC and (b) MnO_2-G and AC electrodes in 0.5 M Na_2SO_4 aqueous electrolyte under galvanostatic cycling at constant current $I = \pm 1$ mA. The potential windows of AC and MoO_2-rGO electrodes ranged from 3.2 to 4 V and 3.3 to 1.2 V vs. Li/Li^+, respectively. On the other hand, the potential windows of MnO_2-G and AC electrodes ranged from 0 to 0.9 V and 0 to -0.9 V vs. Ag/AgCl, respectively. Figures 1(a) and 1(b) indicate that the potential evolution of MoO_2-rGO and MnO_2-G electrodes versus capacity were sloped in a way typical of pseudocapacitive electrodes in absence of phase transformation [4].

Figure 1 also shows the cyclic voltammograms for (c) AC and MoO_2-rGO electrodes in 1 M $LiClO_4$ in 1:1 EC:DMC and (d) MnO_2-G and AC electrodes in 0.5 M Na_2SO_4 aqueous electrolyte at scan rate $\nu = 20$ mV/s. These figures indicates that the CV curve of AC electrodes featured nearly rectangular and symmetrical shape indicating near ideal capacitive behavior. By contrast, the pseudocapacitive MoO_2-rGO electrode featured two redox peaks between 1 and 2.4 V versus Li/Li^+ corresponding to Li^+ intercalation/deintercalation taking place into two different sites along MoO_2 nanoparticles tunnels [8]. On the other hand, MnO_2-G electrode also featured nearly rectangular shape (i.e., no redox peaks) typical of fast surface redox reactions [4]. Note that the current obtained in MoO_2-rGO electrode was nearly three times larger than that in MnO_2-G, illustrating the benefit of intercalation/deintercalation versus fast surface redox reactions for charge storage.

4.2 Hybrid supercapacitors characterization

4.2.1 Cyclic voltammetry

Figure 2 plots the CV curves measured for (a) Device 1, (b) Device 2, and (c) Device 3 for scan rates ν between 10 and 30 mV/s. The open circuit voltage of 0.5 and 0.4 V was used as the minimum potential $\psi_{s,min}$ for AC/MoO_2-rGO (Devices 1 and 2) and MnO_2-G/AC (Device 3), respectively. Based on the individual electrode electrochemical characterization (Figure 1), the maximum potential $\psi_{s,max}$ was taken as 2.5 V for AC/MoO_2-rGO (Devices 1 and 2) and as 1.4 V for MnO_2-G/AC (Device 3). The potential windows prescribed for each device are summarized in Table 1.

Figure 2(a) indicates that the redox peaks observed in the three-electrode measurements for MoO_2-rGO electrode [Figure 1(a)] were retained in Device 1 with $LiClO_4$ electrolyte. Figure 2(a) also shows that the shift in the redox peaks as a function of scan rate was relatively small indicating fast and highly reversible Li^+ intercalation/deintercalation [37]. In addition, the so-called b-value featured a dip in the potential range 1.7 V $< \psi_s <$ 1.9 V corresponding to the transition between capacitive and faradaic regimes (see Supplementary

Materials) [38]. By contrast, Figure 2(b) indicates that the CV curves of AC/MoO_2-rGO cell in $TBABF_4$ (Device 2) did not feature the prominent redox peaks observed in Device 1. In fact, the current was much smaller than that in $LiClO_4$ electrolyte and the CV curves in $TBABF_4$ were nearly rectangular and typical of EDLC behavior. However, a pair of small redox humps was observed around 1.8 V and 1.1 V (indicated by red arrows in Figure 2(b)) during charging and discharging, respectively, suggesting TBA^+ insertion/desertion into the rGO layers [43]. On the other hand, Figure 2(c) indicates that the CV curves of Device 3 with MnO_2-G pseudocapacitive electrode in $NaSO_4$ aqueous electrolyte were nearly rectangular. However, the current was much larger than in Device 2 [Figure 2(b)] due to the contribution of fast surface redox reactions to charge storage [4, 39].

Figure 2(d) plots the charge capacity $C(\nu)$ as a function of scan rate ν for Devices 1, 2, and 3. For all devices, the capacity $C(\nu)$ decreased with increasing scan rate, as typically observed in various electrochemical capacitors [8, 40]. The decrease was sharper for Device 1 than for Device 3. This could be attributed to the relatively slow Li^+ intercalation (Device 1) which could not follow the rapid changes in potential with increasing scan rate, unlike fast surface redox reactions taking place in Device 3. The specific surface area of MoO_2-rGO suggests that the EDL capacity contribution to the total capacity of Devices 1 and 2 was between 0.003 and 0.006 mAh assuming an average electric double-layer capacitance of 10 to 20 $\mu F/cm^2$ [41, 42]. This indicates that the EDL capacity represented less than 20% of the total capacity of Device 1 (AC/MoO_2-rGO in 1 M $LiClO_4$). In other words, Li^+ intercalation contributed significantly more than EDL formation to the total capacity of AC/MoO_2-rGO hybrid supercapacitor. On the other hand, the capacity of Device 2 was 25% larger than the estimated EDL capacity. This may be attributed to the contribution of TBA^+ ions intercalating into the rGO layers [43]. Finally, the capacity of Device 3 (> 0.012 mAh) was much larger than the estimated EDL capacity (between 0.0015 and 0.003 mAh) confirming the fast surface redox contribution. In addition, the b-value of Device 3 was close to unity across the potential window corresponding to fast reversible faradaic reactions (see Supplementary Materials).

4.2.2 Galvanostatic cycling

Figure 3 shows the potential $\psi_s(t)$ across the cell for (a) Device 1 and (b) Device 2 with potential window $(\psi_{s,max} - \psi_{s,min}) = (2.5 - 0.5)$ V and (c) Device 3 with potential window $(\psi_{s,max} - \psi_{s,min}) = (1.4 - 0.4)$ V as a function of time t during galvanostatic cycling with constant current I between 2 and 6 mA. Figure 3(a) indicates that the rate of change in the cell potential $|\mathrm{d}\psi_s/\mathrm{d}t|$ across Device 1 was relatively large at the beginning of the charging step up to $\psi_s \sim 1.9$ V. Beyond this potential, $|\mathrm{d}\psi_s/\mathrm{d}t|$ strongly decreased, resulting in a typical "kink". This "kink" can be attributed to the transition from the capacitive regime to the faradaic regime, as discussed earlier [44]. In the fact, the "kinks" around $\psi_s = 1.9$ V during charging and $\psi_s = 1.7$ V during discharging corresponded to the redox peaks observed in the CV curves around the same potential [Figure 2(a)] and to the dip in the b-value. By contrast, Figure 3(b) indicates that no "kink" was observed when using $TBABF_4$ salt instead of $LiClO_4$ salt in the electrolyte. This observation confirms the suppression of redox reactions with MoO_2 nanoparticles in Device 2. Note also that, for the same imposed current, the charging-discharging time t_{cd} of Device 1 was nearly double that of Device 2. This was due to Li^+ intercalation in MoO_2 of Device 1 resulting in significantly larger charge storage capacity under constant current. Figure 3(c) shows that the potential evolution of Device 3 varied linearly with time, as typically observed in not only EDLCs but also in hybrid pseudocapacitors with fast surface redox reactions [4, 37]. However, here also, the duration of charging/discharging were longer than in Device 2 due to surface redox reactions.

Moreover, Figure 3(d) plots the internal resistance $R_s(I)$ estimated from Equation (7) for Devices 1, 2, and 3 as a function of imposed current I ranging from 2 to 6 mA. In all cases, the internal resistance R_s was nearly independent of current I with average value of (i) $15 \pm 2\ \Omega$ for Device 1, (ii) $27.3 \pm 4\ \Omega$ for Device 2, and (iii) $6.7 \pm 3\ \Omega$ for Device 3. The relatively low resistance of Device 3 can be attributed to the fact that the mass loading of its AC electrode was nearly 40% smaller than that of Devices 1 and 2. The difference in resistance between Device 1 and Device 2 was due to the larger ionic conductivity of 1 M $LiClO_4$ compared with 1 M $TBABF_4$ in EC:DMC due to the smaller size of solvated Li^+

($\sim$ 0.41 nm [45]) compared with TBA^+ ($\sim$ 1.16 nm [25]). For example, the ionic conductivity of 1 M $LiClO_4$ in dimethylformamide (DMF) was 20 mS/cm [46] and was larger than that of 1 M $TBABF_4$ in DMF reported as 14.5 mS/cm [47]. The same trend can be reasonably expected in EC:DMC solvent.

4.3 Instantaneous and irreversible heat generation rates

Figure 4 shows the time-dependent heat generation rates measured at the AC, MoO_2-rGO, and MnO_2-G electrodes denoted by $\dot{Q}_{\mathrm{AC}}(t)$, $\dot{Q}_{\mathrm{MoO_2\text{-}rGO}}(t)$, and $\dot{Q}_{\mathrm{MnO_2\text{-}G}}(t)$ for (a) Device 1, (b) Device 2, and (c) Device 3 as functions of dimensionless time t/t_{cd} for five consecutive galvanostatic cycles under constant current $I = 6$ mA. It also plots the time-dependent heat generation rate $\dot{Q}_T(t)$ in the respective device. The instantaneous heat generation rate at each electrode of all devices was repeatable cycle after cycle. In addition, the magnitude of the heat generation rate $\dot{Q}_i(t)$ at the pseudocapacitive electrodes in all devices was larger than that at the AC counter electrodes. It is interesting to note that $\dot{Q}_{\mathrm{MoO_2\text{-}rGO}}(t)$ was out of phase with $\dot{Q}_{\mathrm{AC}}(t)$ in Device 1, charging by Li^+ intercalation [Figure 4(a)]. However, it was in phase in Device 2, charging mainly by EDL formation of TBA^+ [Figure 4(b)].

Moreover, the instantaneous heat generation rate $\dot{Q}_i(t)$ at electrode "i" is the superposition of an irreversible $\dot{Q}_{irr,i}(t)$ and a reversible $\dot{Q}_{rev,i}(t)$ heat generation rates, i.e., $\dot{Q}_i(t) = \dot{Q}_{irr,i}(t) + \dot{Q}_{rev,i}(t)$. By definition, time-averaging the instantaneous reversible heat generation rate $\dot{Q}_{rev,i}(t)$ at electrode "i" over an entire cycle yields $\bar{\dot{Q}}_{rev,i} = 0$. Thus, the time-averaged irreversible heat generation rate $\bar{\dot{Q}}_{irr,i}$ at electrode "i" subjected to galvanostatic cycling of period t_{cd} (in s) can be expressed as,

$$\bar{\dot{Q}}_{irr,i} = \frac{1}{t_{cd}} \int_{(n-1)t_{cd}}^{nt_{cd}} \dot{Q}_i(t)\ \mathrm{d}t \qquad \text{with } i = \text{ AC, } MoO_2\text{-rGO, or } MnO_2\text{-G} \tag{8}$$

where n is the cycle number taken sufficiently large to have reached oscillatory steady state. Figure 4 shows the time-averaged irreversible heat generation rate $\bar{\dot{Q}}_{irr,i}$ at the AC, MoO_2-rGO, and MnO_2-G electrodes and in the entire cell for (d) Device 1, (e) Device 2, and (f) Device 3 under galvanostatic cycling as functions of I^2 for current I ranging between 2 and

6 mA. The error bars correspond to two standard deviations or 95% confidence interval estimated by evaluating $\bar{\dot{Q}}_{irr,i}$ over five consecutive galvanostatic cycles. First, Figures 4(d)-4(f) indicate that the irreversible heat generation rate $\bar{\dot{Q}}_{irr,\mathrm{AC}}$ in the AC electrodes was positive and linearly proportional to I^2 in all devices. These results suggest that Joule heating was the dominant source of irreversible heat generation in the AC electrodes. The same conclusion was reached previously both experimentally [16–18, 48] and numerically for carbon-based EDLC devices [20, 49]. It was also reached numerically for AC electrode in hybrid supercapacitors [20]. Then, the coefficient of proportionality between $\bar{\dot{Q}}_{irr,\mathrm{AC}}$ and I^2 corresponds to the AC half-cell resistance R_{AC}, i.e., $\bar{\dot{Q}}_{irr,\mathrm{AC}} = R_{\mathrm{AC}} I^2$. Least square fitting of the experimental data yields $R_{\mathrm{AC}} = 8.4$, 9.9, and 4.5 Ω for Devices 1, 2, and 3, respectively. The resistances R_{AC} of Devices 1 and 2 were similar since the mass loading and synthesis of the AC electrodes in each device were identical. The differences between R_{AC} of Devices 1 and 2 can be attributed to the fact that $TBABF_4$ has a smaller ionic conductivity than $LiClO_4$, as previously discussed. On the other hand, the resistance R_{AC} of Device 3 was nearly half that of Devices 1 and 2 due to the smaller mass loading and to the fact that aqueous Na_2SO_4 electrolyte had larger electrical conductivity ($\sim$ 60 mS/cm [50]) than the organic electrolytes used in Devices 1 and 2.

Moreover, Figures 4(d)-4(f) establishes that the time-averaged total irreversible heat generation rate $\bar{\dot{Q}}_{irr,T}$ in the entire devices exceeded the heat generation rate due to Joule heating denoted by $\bar{\dot{Q}}_J$ and given by [51],

$$\bar{\dot{Q}}_J = R_s \; I^2 \tag{9}$$

where R_s is the device internal resistance estimated from the IR drop and found to be independent of current [Figure 3(d)]. The deviation between $\bar{\dot{Q}}_{irr,T}$ and $\bar{\dot{Q}}_J$ was more significant in Device 1 and Device 3 than in Device 2. In addition, $\bar{\dot{Q}}_{irr,T}$ deviated significantly from $\bar{\dot{Q}}_J$ at low currents when the faradaic charge storage dominated [20]. These observations can be attributed to polarization heating [20, 21]. In addition, the redox reactions at the pseudocapacitive electrode surface could cause hysteresis in EDL formation resulting in additional contribution to the irreversible heat generation rate, as previously discussed [20].

4.4 Reversible heat generation rate

4.4.1 Activated carbon electrodes

The instantaneous reversible heat generation rate $\dot{Q}_{rev,\mathrm{AC}}(t)$ (in mW) in the AC half-cell under constant current cycling can be expressed as [17, 18],

$$\dot{Q}_{rev,\mathrm{AC}}(t) = \dot{Q}_{\mathrm{AC}}(t) - \dot{Q}_{irr,\mathrm{AC}}(t) = \dot{Q}_{\mathrm{AC}}(t) - R_{\mathrm{AC}} I^2. \tag{10}$$

This analysis takes advantage of the facts that (a) the instantaneous irreversible heat generation rate $\dot{Q}_{irr,\mathrm{AC}}(t)$ is independent of time under constant current cycling, i.e., $\dot{Q}_{irr,\mathrm{AC}}(t) = \bar{\dot{Q}}_{irr,\mathrm{AC}}$ and (b) the resistance R_{AC} of the AC half-cell can be estimated by time-averaging $\dot{Q}_{\mathrm{AC}}(t)$ over a cycle (Figure 4), i.e., $\bar{\dot{Q}}_{irr,\mathrm{AC}} = R_{\mathrm{AC}} I^2$. In addition, the time-averaged reversible heat generation rates during the charging step $\bar{\dot{Q}}^{c}_{rev,\mathrm{AC}}$ at the AC electrode can be calculated as [17, 18],

$$\bar{\dot{Q}}^{c}_{rev,\mathrm{AC}} = \frac{1}{t_c} \int_{(n-1)t_{cd}}^{(n-1)t_{cd}+t_c} \dot{Q}_{rev,\mathrm{AC}}(t)\ \mathrm{d}t. \tag{11}$$

where t_c is the duration of the charging step.

Figure 5(a) plots $\dot{Q}_{rev,\mathrm{AC}}(t)$ as a function of dimensionless time t/t_{cd} for Devices 1, 2, and 3 for current $I = 6$ mA. Similar trends were observed for other values of imposed current I (see Supplementary Materials). Figure 5 indicates that, for all devices, $\dot{Q}_{rev,\mathrm{AC}}(t)$ was exothermic during charging due to ion adsorption and endothermic during discharging due to ion desorption. Indeed, the reversible adsorption process reduces the entropy S of the system ($\mathrm{d}S/\mathrm{d}t < 0$) as ions arrange from a disordered to an ordered state to form the EDL at the electrolyte/electrode interface. In addition, our calorimeter imposed isothermal conditions in the device such that $\dot{Q}_{rev} = T\mathrm{d}S/\mathrm{d}t < 0$, i.e., the system releases heat and ion adsorption is exothermic. Conversely, during discharging, reversible ions desorption is endothermic. Note that the above findings were consistent with (i) previous experimental studies [16,17,48] and (ii) numerical predictions for reversible heat generation in carbon-based EDLCs [49] and in hybrid supercapacitors [20]. Although the heat generation rates $\dot{Q}_{rev,\mathrm{AC}}(t)$ in the three devices were in phase and had similar magnitudes, their temporal evolution were

slightly different. Also, minor differences have been observed in the thermal behavior between $\dot{Q}_{rev,\mathrm{AC}}(t)$ in EDLC [49] and in hybrid supercapacitors [20]. This could be attributed to the fact that the charging/discharging behavior (e.g., potential window, concentration, charging rate) of AC electrodes is affected by charging of the pseudocapacitive counter electrodes [52]. Indeed, the cell potential may not split evenly between the pseudocapacitive and AC electrodes due to differences in their capacity [52].

Figure 5(b) plots the time-averaged reversible heat generation rates during the charging step $\bar{\dot{Q}}^{c}_{rev,\mathrm{AC}}$ at the AC electrode as a function of current I ranging between 2 and 6 mA for Devices 1, 2, and 3 (Table 1). Here also, the reported values of $\bar{\dot{Q}}^{c}_{rev,\mathrm{AC}}$ were averaged over 5 consecutive cycles and the error bars corresponded to 95% confidence interval. First, Figure 5(b) indicates that, for all three devices, the time-averaged reversible heat generation rate $\bar{\dot{Q}}^{c}_{rev,\mathrm{AC}}$ at the AC electrode was positive and nearly proportional to current I. This observation was also consistent with experimental measurements [16–18] and numerical simulations for EDLC electrodes [49, 53]. Note that charging of Device 2 at 5 and 6 mA was less than 3.5 s due to its much smaller capacity (Figure 2(d)). Then, the charging time was not significantly larger than the response time of the calorimeter of 0.7 s [17]. This caused significant uncertainty in the values of $\bar{\dot{Q}}_{rev,\mathrm{AC}}$ which were not reported in Figure 5(b).

4.4.2 Pseudocapacitive electrodes

Unlike for AC electrodes [17, 18], the instantaneous reversible heat generation rate $\dot{Q}_{rev,\mathrm{P}}(t)$ at the pseudocapacitive electrodes of Devices 1 and 3 could not be easily retrieved because the irreversible contribution $\dot{Q}_{irr,\mathrm{P}}(t)$ was likely time-dependent and unknown. Thus, Equation (10) could not be transposed to pseudocapacitive electrodes. Indeed, the instantaneous irreversible heat generation associated with redox reactions strongly depends on the time-dependent overpotential of the pseudocapacitive electrode [20]. Nevertheless, Joule heating $\dot{Q}_{J,\mathrm{P}}$ at the pseudocapacitive half-cell can still be evaluated under constant current charging/discharging according to,

$$\dot{Q}_{J,\mathrm{P}}(t) = R_{\mathrm{P}} I^2 \tag{12}$$

where R_{P} is the resistance of the pseudocapacitive half-cell estimated as $R_{\mathrm{P}} = R_s - R_{\mathrm{AC}}$. Then, $\dot{Q}_{J,\mathrm{P}}(t)$ can be subtracted from the instantaneous heat generation $\dot{Q}_{\mathrm{P}}(t)$ at the pseudocapacitive electrode to obtain the heat generation rate $\dot{Q}_{other,\mathrm{P}}(t)$ associated with phenomena other than Joule heating taking place at the pseudocapacitive electrode including contribution from EDL formation and redox reactions with or without intercalation/deintercalation, i.e.,

$$\dot{Q}_{other,\mathrm{P}}(t) = \dot{Q}_{\mathrm{P}}(t) - \dot{Q}_{J,\mathrm{P}}(t) = \dot{Q}_{\mathrm{P}}(t) - R_{\mathrm{P}} I^2. \tag{13}$$

Figure 6(a) plots $\dot{Q}_{other,\mathrm{P}}(t)$ and the corresponding potential evolution $\psi_s(t)$ at the pseudocapacitive electrode as functions of dimensionless time t/t_{cd} for Devices 1, 2, and 3 for current $I = 6$ mA. Similar trends were observed for other currents (see Supplementary Materials). First, Figure 6(a) indicates that the thermal behavior of the pseudocapacitive electrodes was significantly different from one device to another due to differences in the charging mechanisms. Here, $\dot{Q}_{other,\mathrm{P}}(t)$ in Device 1 can be described as the superposition of irreversible and reversible heat generation associated with EDL formation and redox reactions. By definition, the irreversible faradaic contribution $\dot{Q}_{irr,F}$ was exothermic during charging and discharging steps as the current I and overpotential η have always the same sign, i.e., $\dot{Q}_{irr,F} = \eta I$ [20]. Also, the reversible heat generation associated with EDL formation was exothermic during charging based on the fact that ions adsorption process is exothermic [16–18, 48, 49]. However, $\dot{Q}_{other,\mathrm{P}}(t)$ in Device 1 was endothermic (i.e., $\dot{Q}_{other,\mathrm{P}}(t) < 0$) during charging for potential above $\psi_s \sim 1.9$V. This potential corresponded to the transition from the capacitive to the faradaic regimes observed in CV curves and in the $b-$value. This observation indicates that the reversible heat generation associated with redox reactions was endothermic and dominated in the faradaic regime. During discharging, $\dot{Q}_{other,\mathrm{P}}(t)$ in Device 1 was mainly exothermic (i.e., $\dot{Q}_{other,\mathrm{P}}(t) > 0$) due to the irreversible heat generation associated with redox reactions. This indicates that the endothermic contribution from the reversible heat generation associated with ion desorption was insignificant in Device 1. Finally, $\dot{Q}_{other,\mathrm{P}}(t)$ at the MoO_2-rGO electrode of Device 2 behave as an AC electrode except for endothermic process at the begin of the charging step. This behavior could be attributed to TBA^+ intercalation

into the rGO layers [43].

Finally, in order to effectively compare the reversible heat generation rates in the pseudocapacitive electrodes, the time-averaged reversible heat generation rate $\bar{\dot{Q}}^{c}_{rev,P}$ (in mW) during a galvanostatic charging step of duration t_c was derived as (see Supplementary Materials),

$$\bar{\dot{Q}}^{c}_{rev,\mathrm{P}} = \frac{1}{t_c} \int_{(n-1)t_{cd}}^{(n-1)t_{cd}+t_c} \dot{Q}_{other,\mathrm{P}}(t)\ \mathrm{d}t - \bar{\dot{Q}}_{other,irr,\mathrm{P}}. \tag{14}$$

where $\bar{\dot{Q}}_{other,irr,\mathrm{P}}$ is the time-averaged irreversible heat generation rate at the pseudocapacitive electrode excluding Joule heating. Figure 6(b) shows the time-averaged reversible heat generation rate $\bar{\dot{Q}}^{c}_{rev,\mathrm{P}}$ during the charging step at the pseudocapacitive electrode as a function of current I for Devices 1, 2, and 3. It indicates that $\bar{\dot{Q}}^{c}_{rev,\mathrm{P}}$ differed significantly from one device to another. This can be attributed to differences in their charging mechanisms. In fact, several physicochemical phenomena contributed to the reversible heat generation at the pseudocapacitive electrodes including (i) EDL formation [16, 17, 49], (ii) fast surface redox reactions [16, 20], and/or (iii) redox reactions with ions intercalation/deintercalation [4].

MoO_2-rGO electrode. During charging of the MoO_2-rGO pseudocapacitive electrode of Device 1, $Mo^{(IV)}O_2$ reduced to $Mo^{(III)}O_2$ and Li^+ intercalated into the crystalline structure of $Mo^{(III)}O_2$ electrode [8]. In Device 1, $\bar{\dot{Q}}^{c}_{rev,\mathrm{MoO_2\text{-}rGO}}$ was negative [Figure 6(b)] indicating that the reversible heat generation rate was endothermic during charging. To explore the effect of Li^+ intercalation into MoO_2-rGO electrode, an identical device (Device 2) was tested in an electrolyte with non-reacting TBA^+ cations. As expected, the time-averaged reversible heat generation rate at MoO_2-rGO electrode in $TBABF_4$ was exothermic during charging due to ion adsorption and EDL formation, as previously observed in AC electrodes (Figure 5) and in the literature [16–18, 49, 53]. These observations combined with those for Device 1 establish that reversible Li^+ intercalation into MoO_2-rGO electrode was endothermic while Li^+ deintercalation was exothermic.

MnO_2-G electrode. EDL formation and fast surface redox reactions contributed to the reversible heat generation in the MnO_2-G electrode of Device 3. The contribution from

fast surface redox reactions depends on the reaction stoichiometry. The oxidation state of MnO_2 is typically ~ 4 ($Mn^{(IV)}O_2$) in as-prepared electrodes [15, 54]. After assembly in 0.5 M Na_2SO_4, $Mn^{(IV)}$ reduced spontaneously to $Mn^{(III)}$ or to $Mn^{(II)}$, in some cases, according to Pourbaix diagram of Mn-H_2O system at 0 V versus a saturated calomel electrode (SCE) (0.045 V vs. Ag/AgCl) at pH ~ 7 [15, 54, 55]. During this process, Na^+ adsorbed to the MnO_2-G electrode surface. The oxidation state of MnO_2 alternates between IV and III upon charging (Na^+ desorption) and discharging (Na^+ adsorption), respectively. From a thermodynamic viewpoint, the charging process is not spontaneous and thus endothermic. Indeed, in the vast majority of cases, spontaneous reactions are exothermic and non-spontaneous reactions are endothermic [56]. Here, in Device 3, MnO_2-G served as a positive electrode and charged by Na^+ desorption and fast surface redox reactions [Equation (2)]. Figure 6(b) confirms that the time-averaged reversible heat generation in MnO_2-G electrode was endothermic ($\bar{\dot{Q}}^c_{rev,\mathrm{MnO_2\text{-}G}} < 0$) during charging. This has previously been observed experimentally [16] and predicted numerically [20] for MnO_2 pseudocapacitive electrode serving as a positive electrode.

Figure 6(b) also shows that $\bar{\dot{Q}}^c_{rev,\mathrm{MoO_2\text{-}rGO}}$ at the MoO_2-rGO electrode in $LiClO_4$ (Device 1) and $\bar{\dot{Q}}^c_{rev,\mathrm{MnO_2\text{-}G}}$ at the MnO_2-G electrode in Na_2SO_4 (Device 3) were negative and their magnitude increased with increasing current I at low current. They then reached a plateau beyond 4 mA. This can be attributed to the competing effect between EDL formation (exothermic) and redox reactions (endothermic) as EDL formation contributed appreciably to charging at higher currents [20]. Similarly, $\bar{\dot{Q}}^c_{rev,\mathrm{MoO_2\text{-}rGO}}$ at MoO_2-rGO in $TBABF_4$ (Device 2) was independent of current I unlike in AC electrode when it was linearly proportional to I. This observation could potentially be due to competing effects between EDL formation (exothermic) [49] and partially reversible TBA^+ intercalation into the rGO (endothermic) [57]. In addition, rGO could undergo partially reversible volumetric expansion upon charging due to the large size of intercalated TBA^+ ions into the restacked layers of rGO [43]. Such volumetric expansion could also contribute negatively to the heat generation since the elongation of C-C bond is an endothermic process [57].

5 Conclusion

The present study investigated the thermal behavior associated with two pseudocapacitive charge storage mechanisms involving redox reactions namely Li^+ intercalation and fast surface redox reactions. To do so, a custom-made *in operando* calorimeter was used to measure the time-dependent heat generation rate in each electrode of hybrid supercapacitors consisting of MoO_2-rGO (charged by Li^+ intercalation) or MnO_2-G (charged by fast surface redox reactions) with an over-sized AC as a counter electrode. A data analysis procedure was developed to facilitate interpretation and distinguish between irreversible and reversible heat generation rates. First, the devices were characterized using cyclic voltammetry and galvanostatic cycling. Second, for all devices, the measured time-averaged irreversible heat generation rate at the AC electrode was proportional to I^2 and attributed to Joule heating. By contrast, the total irreversible heat generation rates measured in the pseudocapacitive electrodes exceeded Joule heating due to irreversible heat generation associated with redox reactions, polarization heating, and hysteresis in EDL formation/dissolution. Finally, the time-averaged reversible heat generation over a charging step at the AC electrodes was systematically exothermic during charging and nearly proportional to I. By contrast, MoO_2-rGO electrode in $LiClO_4$ organic electrolyte featured endothermic reversible heat generation during charging due to Li^+ intercalation into MoO_2-rGO. This was confirmed by using an electrolyte with larger cations, i.e., $TBABF_4$ responsible for suppressing redox reactions and intercalation. Also, MnO_2-G electrode in aqueous Na_2SO_4 electrolyte featured endothermic heat generation during charging due to non-spontaneous redox reactions.

Acknowledgment

O.M. is grateful for the financial support provided by King Fahd University of Petroleum and Minerals (KFUPM), Dhahran, Saudi Arabia. J.L., C.S.C., D.B., and B.D. were supported by the Office of Naval Research (under Grant N00014-16-1-2164). B.M. was supported by the China Scholarship Council.

References

[1] B. Conway, *Electrochemical Supercapacitors: Scientific Fundamentals and Technological Applications*, Kluwer Academic/Plenum, New York, NY, 1999.

[2] B. E. Conway, V. Birss, and J. Wojtowicz, "The role and utilization of pseudocapacitance for energy storage by supercapacitors", *Journal of Power Sources*, vol. 66, no. 1-2, pp. 1–14, 1997.

[3] T. Brousse, D. Belanger, and J. W. Long, "To be or not to be pseudocapacitive?", *Journal of the Electrochemical Society*, vol. 162, no. 5, pp. A5185–A5189, 2015.

[4] M. R. Lukatskaya, B. Dunn, and Y. Gogotsi, "Multidimensional materials and device architectures for future hybrid energy storage", *Nature Communications*, vol. 7, pp. 1–13, 2016.

[5] S. K. Jung, H. Gwon, J. Hong, K. Y. Park, D. H. Seo, H. Kim, J. Hyun, W. Yang, and K. Kang, "Understanding the degradation mechanisms of $LiNi_{0.5}Co_{0.2}Mn_{0.3}O_2$ cathode material in lithium ion batteries", *Advanced Energy Materials*, vol. 4, no. 1, pp. 1–7, 2014.

[6] V. Augustyn, P. Simon, and B. Dunn, "Pseudocapacitive oxide materials for high-rate electrochemical energy storage", *Energy and Environmental Science*, vol. 7, no. 5, pp. 1597–1614, 2014.

[7] M. Toupin, T. Brousse, and D. Belanger, "Charge storage mechanism of MnO_2 electrode used in aqueous electrochemical capacitor", *Chemistry of Materials*, vol. 16, no. 16, pp. 3184–3190, 2004.

[8] H.-S. Kim, J. B. Cook, S. H. Tolbert, and B. Dunn, "The development of pseudocapacitive properties in nanosized-MoO_2", *Journal of the Electrochemical Society*, vol. 162, no. 5, pp. A5083–A5090, 2015.

[9] J. Yan, Z. Fan, T. Wei, W. Qian, M. Zhang, and F. Wei, "Fast and reversible surface redox reaction of graphene-MnO_2 composites as supercapacitor electrodes", *Carbon*, vol. 48, no. 13, pp. 3825–3833, 2010.

[10] L. C. Yang, Q. S. Gao, Y. Tang, Y. P. Wu, and R. Holze, "MoO_2 synthesized by reduction of MoO_3 with ethanol vapor as an anode material with good rate capability for the lithium ion battery", *Journal of Power Sources*, vol. 179, no. 1, pp. 357–360, 2008.

[11] Y. Shi, B. Guo, S. A. Corr, Q. Shi, Y. S. Hu, K. R. Heier, L. Chen, R. Seshadri, and G. D. Stucky, "Ordered mesoporous metallic MoO_2 materials with highly reversible lithium storage capacity", *Nano Letters*, vol. 9, no. 12, pp. 4215–4220, 2009.

[12] B. Guo, X. Fang, B. Li, Y. Shi, C. Ouyang, Y. S. Hu, Z. Wang, G. D. Stucky, and L. Chen, "Synthesis and lithium storage mechanism of ultrafine MoO_2 nanorods", *Chemistry of Materials*, vol. 24, no. 3, pp. 457–463, 2012.

[13] D. Belanger, T. Brousse, and J. W. Long, "Manganese oxides: Battery materials make the leap to electrochemical capacitors", *Electrochemical Society Interface*, vol. 17, no. 1, pp. 49–52, 2008.

[14] P. Ragupathy, H. N. Vasan, and N. Munichandraiah, "Synthesis and characterization of nano-MnO_2 for electrochemical supercapacitor studies", *Journal of The Electrochemical Society*, vol. 155, no. 1, pp. A34–A40, 2008.

[15] P. Iamprasertkun, A. Krittayavathananon, A. Seubsai, N. Chanlek, P. Kidkhunthod, W. Sangthong, S. Maensiri, R. Yimnirun, S. Nilmoung, P. Pannopard, S. Ittisanronnachai, K. Kongpatpanich, J. Limtrakul, and M. Sawangphruk, "Charge storage mechanisms of manganese oxide nanosheets and N-doped reduced graphene oxide aerogel for high-performance asymmetric supercapacitors", *Scientific Reports*, vol. 6, pp. 1–12, 2016.

[16] Y. Dandeville, P. Guillemet, Y. Scudeller, O. Crosnier, L. Athouel, and T. Brousse, "Measuring time-dependent heat profiles of aqueous electrochemical capacitors under cycling", *Thermochimica Acta*, vol. 526, no. 1-2, pp. 1–8, 2011.

[17] O. Munteshari, J. Lau, A. Krishnan, B. Dunn, and L. Pilon, "Isothermal calorimeter for measurements of time-dependent heat generation rate in individual supercapacitor electrodes", *Journal of Power Sources*, vol. 374, pp. 257–268, 2018.

[18] O. Munteshari, J. Lau, D. S. Ashby, B. Dunn, and L. Pilon, "Effects of constituent materials on heat generation in individual EDLC electrodes", *Journal of The Electrochemical Society*, vol. 165, no. 7, pp. 1547–1557, 2018.

[19] A. Likitchatchawankun, A. Kundu, O. Munteshari, T. S. Fisher, and L. Pilon, "Heat generation in all-solid-state supercapacitors with graphene electrodes and gel electrolytes", *Electrochimica Acta*, vol. 303, pp. 341–353, 2019.

[20] A. L. d'Entremont and L. Pilon, "First-principles thermal modeling of hybrid pseudocapacitors under galvanostatic cycling", *Journal of Power Sources*, vol. 335, pp. 172–188, 2016.

[21] Q. Wang, Q. Sun, P. Ping, X. Zhao, J. Sun, and Z. Lin, "Heat transfer in the dynamic cycling of lithium-titanate batteries", *International Journal of Heat and Mass Transfer*, vol. 93, pp. 896–905, 2016.

[22] W. S. Hummers and R. E. Offeman, "Preparation of graphitic oxide", *Journal of the American Chemical Society*, vol. 80, no. 6, pp. 1939–1939, 1958.

[23] L. J. Cote, F. Kim, and J. Huang, "Langmuir-Blodgett assembly of graphite oxide single layers", *Journal of the American Chemical Society*, vol. 131, no. 3, pp. 1043–1049, 2009.

[24] I. Pineiro-Prado, D. Salinas-Torres, R. Ruiz-Rosas, E. Morallon, and D. Cazorla-Amoros, "Design of activated carbon/activated carbon asymmetric capacitors", *Frontiers in Materials*, vol. 3, pp. 1–12, 2016.

[25] C. J. Huang, I. Favre, and E. G. Moczydlowski, "Permeation of large tetra-alkylammonium cations through mutant and wild-type voltage-gated sodium channels as revealed by relief of block at high voltage", *The Journal of General Physiology*, vol. 115, no. 4, pp. 435–54, 2000.

[26] S. H. Lapidus, N. N. Rajput, X. Qu, K. W. Chapman, K. A. Persson, and P. J. Chupas, "Solvation structure and energetics of electrolytes for multivalent energy storage", *Physical Chemistry Chemical Physics*, vol. 16, no. 40, pp. 21941–21945, 2014.

[27] T. Brezesinski, J. Wang, S. H. Tolbert, and B. Dunn, "Ordered mesoporous α-MoO_3 with iso-oriented nanocrystalline walls for thin-film pseudocapacitors", *Nature Materials*, vol. 9, no. 2, pp. 146–151, 2010.

[28] Z. Yang, H. Guo, X. Li, Z. Wang, Z. Yan, and Y. Wang, "Natural sisal fibers derived hierarchical porous activated carbon as capacitive material in lithium ion capacitor", *Journal of Power Sources*, vol. 329, pp. 339–346, 2016.

[29] S. Brunauer, P. H. Emmett, and E. Teller, "Adsorption of gases in multimolecular layers", *Journal of the American Chemical Society*, vol. 60, no. 2, pp. 309–319, 1938.

[30] M. Kruk and M. Jaroniec, "Gas adsorption characterization of ordered organic-inorganic nanocomposite materials", *Chemistry of Materials*, vol. 13, no. 10, pp. 3169–3183, 2001.

[31] GreenTEG, *Instruction Manual for gSKIN Heat Flux Sensors for R&D*, https://shop.greenteg.com/wp-content/uploads/gSKIN_Heat-Flux-Sensors-RD_Instructions_v2.pdf. Last accessed in Dec. 2018.

[32] R. T. Wen, C. G. Granqvist, and G. A. Niklasson, "Eliminating degradation and uncovering ion-trapping dynamics in electrochromic WO_3 thin films", *Nature Materials*, vol. 14, no. 10, pp. 996–1001, 2015.

[33] A. Burke and M. Miller, "Testing of electrochemical capacitors: Capacitance, resistance, energy density, and power capability", *Electrochimica Acta*, vol. 55, no. 25, pp. 7538–7548, 2010.

[34] S. Zhao, F. Wu, L. Yang, L. Gao, and A. Burke, "A measurement method for determination of dc internal resistance of batteries and supercapacitors", *Electrochemistry Communications*, vol. 12, no. 2, pp. 242–245, 2010.

[35] M. Stoller and R. Ruoff, "Best practice methods for determining an electrode material's performance for ultracapacitors", *Energy & Environmental Science*, vol. 3, no. 9, pp. 1294–1301, 2010.

[36] B.-A. Mei, O. Munteshari, J. Lau, B. Dunn, and L. Pilon, "Physical interpretations of Nyquist plots for EDLC electrodes and devices", *Journal of Physical Chemistry C*, vol. 122, no. 1, pp. 194–206, 2018.

[37] J. B. Cook, H. S. Kim, Y. Yan, J. S. Ko, S. Robbennolt, B. Dunn, and S. H. Tolbert, "Mesoporous MoS_2 as a transition metal dichalcogenide exhibiting pseudocapacitive Li and Na-ion charge storage", *Advanced Energy Materials*, vol. 6, no. 9, pp. 1501937 (1–12), 2016.

[38] H. L. Girard, H. Wang, A. L. d'Entremont, and L. Pilon, "Physical interpretation of cyclic voltammetry for hybrid pseudocapacitors", *Journal of Physical Chemistry C*, vol. 119, no. 21, pp. 11349–11361, 2015.

[39] O. Ghodbane, J. L. Pascal, and F. Favier, "Microstructural effects on charge-storage properties in MnO_2-based electrochemical supercapacitors", *ACS Applied Materials and Interfaces*, vol. 1, no. 5, pp. 1130–1139, 2009.

[40] C. H. Lai, D. Ashby, M. Moz, Y. Gogotsi, L. Pilon, and B. Dunn, "Designing pseudocapacitance for Nb_2O_5/carbide-derived carbon electrodes and hybrid devices", *Langmuir*, vol. 33, no. 37, pp. 9407–9415, 2017.

[41] J. Chmiola, G. Yushin, Y. Gogotsi, C. Portet, P. Simon, and P. L. Taberna, "Anomalous increase in carbon at pore sizes less than 1 nanometer", *Science*, vol. 313, no. 5794, pp. 1760–1763, 2006.

[42] P. Simon and A. Burke, "Nanostructured carbons: Double-layer capacitance and more", *The Electrochemical Society Interface*, vol. 17, no. 2, pp. 38–43, 2008.

[43] A. J. Cooper, M. Velický, I. A. Kinloch, and R. A.W. Dryfe, "On the controlled electrochemical preparation of R_4N^+ graphite intercalation compounds and their host structural deformation effects", *Journal of Electroanalytical Chemistry*, vol. 730, pp. 34–40, 2014.

[44] A. L. d'Entremont, H.-L. Girard, H. Wang, and L. Pilon, "Electrochemical transport phenomena in hybrid pseudocapacitors under galvanostatic cycling", *Journal of the Electrochemical Society*, vol. 163, no. 2, pp. A229–A243, 2015.

[45] S. H. Lapidus, N. N. Rajput, X. Qu, K. W. Chapman, K. A. Persson, and P. J. Chupas, "Solvation structure and energetics of electrolytes for multivalent energy storage", *Physical Chemistry Chemical Physics*, vol. 16, no. 40, pp. 21941–21945, 2014.

[46] M. Ue, "Electrochemical properties of organic liquid electrolytes based on quaternary onium salts for electrical double-layer capacitors", *Journal of the Electrochemical Society*, vol. 141, no. 11, pp. 2989, 1994.

[47] H. O. House, E. Feng, and N. P. Peet, "A comparison of various tetraalkylammonium salts as supporting electrolytes in organic electrochemical reactions", *Journal of Organic Chemistry*, vol. 36, no. 16, pp. 2371–2375, 1971.

[48] J. Schiffer, D. Linzen, and D. Sauer, "Heat generation in double layer capacitors", *Journal of Power Sources*, vol. 160, no. 1, pp. 765–772, 2006.

[49] A. L. d'Entremont and L. Pilon, "First-principles thermal modeling of electric double layer capacitors under constant-current cycling", *Journal of Power Sources*, vol. 246, pp. 887–898, 2014.

[50] W. Wu, S. Shabhag, J. Chang, A. Rutt, and J. F. Whitacre, "Relating electrolyte concentration to performance and stability for $NaTi_2(PO_4)_3/Na_{0.44}MnO_2$ aqueous sodium-ion batteries", *Journal of the Electrochemical Society*, vol. 162, no. 6, pp. A803–A808, 2015.

[51] R. Mahamud and C. Park, "Reciprocating air flow for Li-ion battery thermal management to improve temperature uniformity", *Journal of Power Sources*, vol. 196, no. 13, pp. 5685–5696, 2011.

[52] S. Roldán, D. Barreda, M. Granda, R. Menéndez, R. Santamaría, and C. Blanco, "An approach to classification and capacitance expressions in electrochemical capacitors technology", *Physical Chemistry Chemical Physics*, vol. 17, no. 2, pp. 1084–1092, 2015.

[53] A. L. d'Entremont and L. Pilon, "Thermal effects of asymmetric electrolytes in electric double layer capacitors", *Journal of Power Sources*, vol. 273, pp. 196–209, 2015.

[54] C. Tanggarnjanavalukul, N. Phattharasupakun, K. Kongpatpanich, and M. Sawangphruk, "Charge storage performances and mechanisms of MnO_2 nanospheres, nanorods, nanotubes and nanosheets", *Nanoscale*, vol. 9, no. 36, pp. 13630–13639, 2017.

[55] W. Wei, X. Cui, W. Chen, and D. G. Ivey, "Improved electrochemical impedance response induced by morphological and structural evolution in nanocrystalline MnO_2 electrodes", *Electrochimica Acta*, vol. 54, no. 8, pp. 2271–2275, 2009.

[56] A. Burrows, J. Holman, A. Parsons, G. Pilling, and G. Price, *Chemistry^3: introducing inorganic, organic and physical chemistry*, Oxford University Press, Oxford, UK, 2017.

[57] Z. Wang, S. M. Selbach, and T. Grande, "Van der Waals density functional study of the energetics of alkali metal intercalation in graphite", *RSC Advances*, vol. 4, no. 8, pp. 4069–4079, 2014.

List of Tables

List of Figures

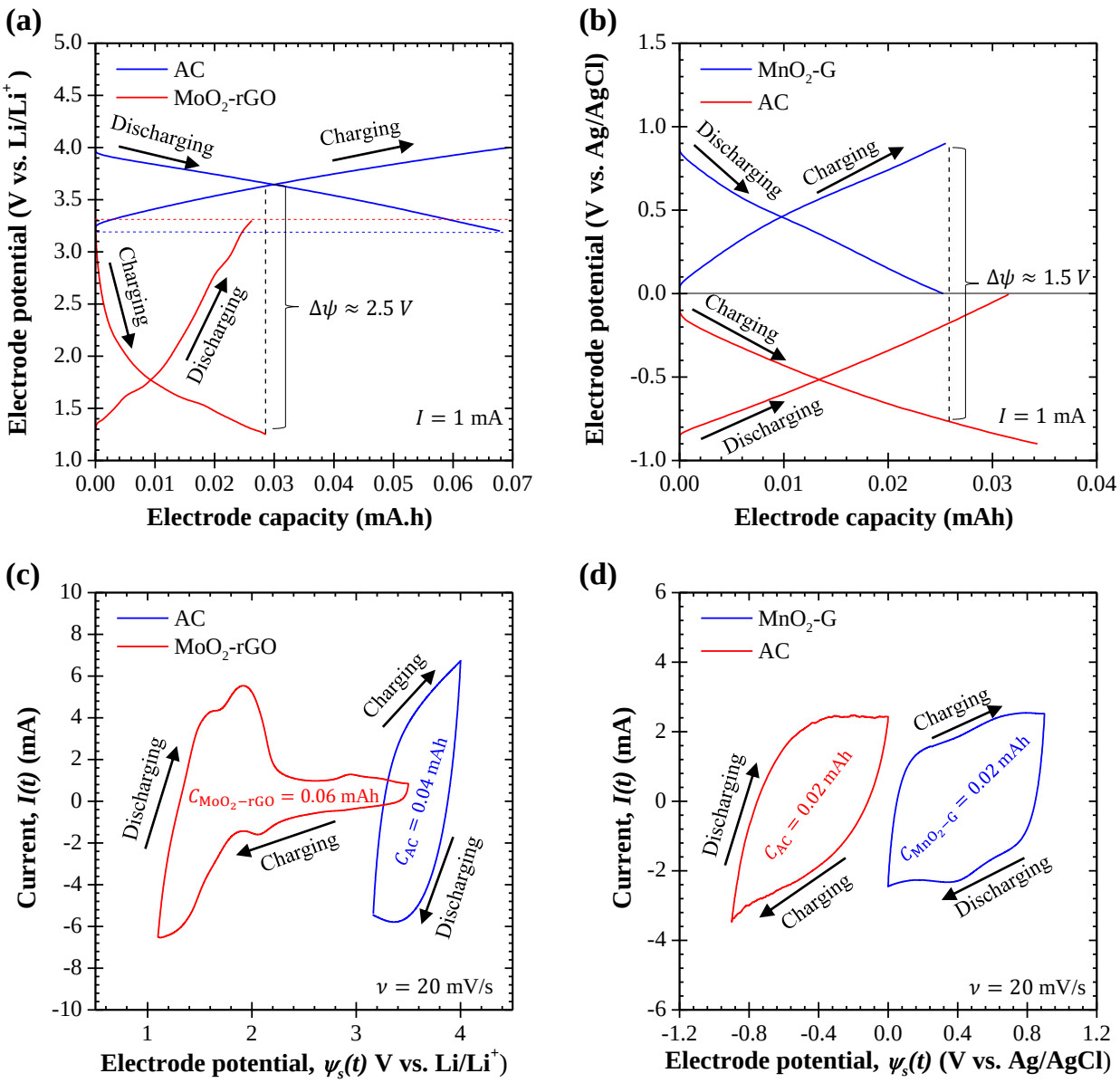

Figure 1: Potential evolution versus capacity from three-electrode measurements for (a) AC and MoO_2-rGO electrodes in 1 M $LiClO_4$ in 1:1 EC:DMC and (b) MnO_2-G and AC electrodes in 0.5 M Na_2SO_4 aqueous electrolyte under galvanostatic cycling at constant current $I = \pm 1$ mA. Cyclic voltammograms for (c) AC and MoO_2-rGO electrodes in 1 M $LiClO_4$ in 1:1 EC:DMC and (d) MnO_2-G and AC electrodes in 0.5 M Na_2SO_4 aqueous electrolyte at scan rate $\nu = 20$ mV/s.

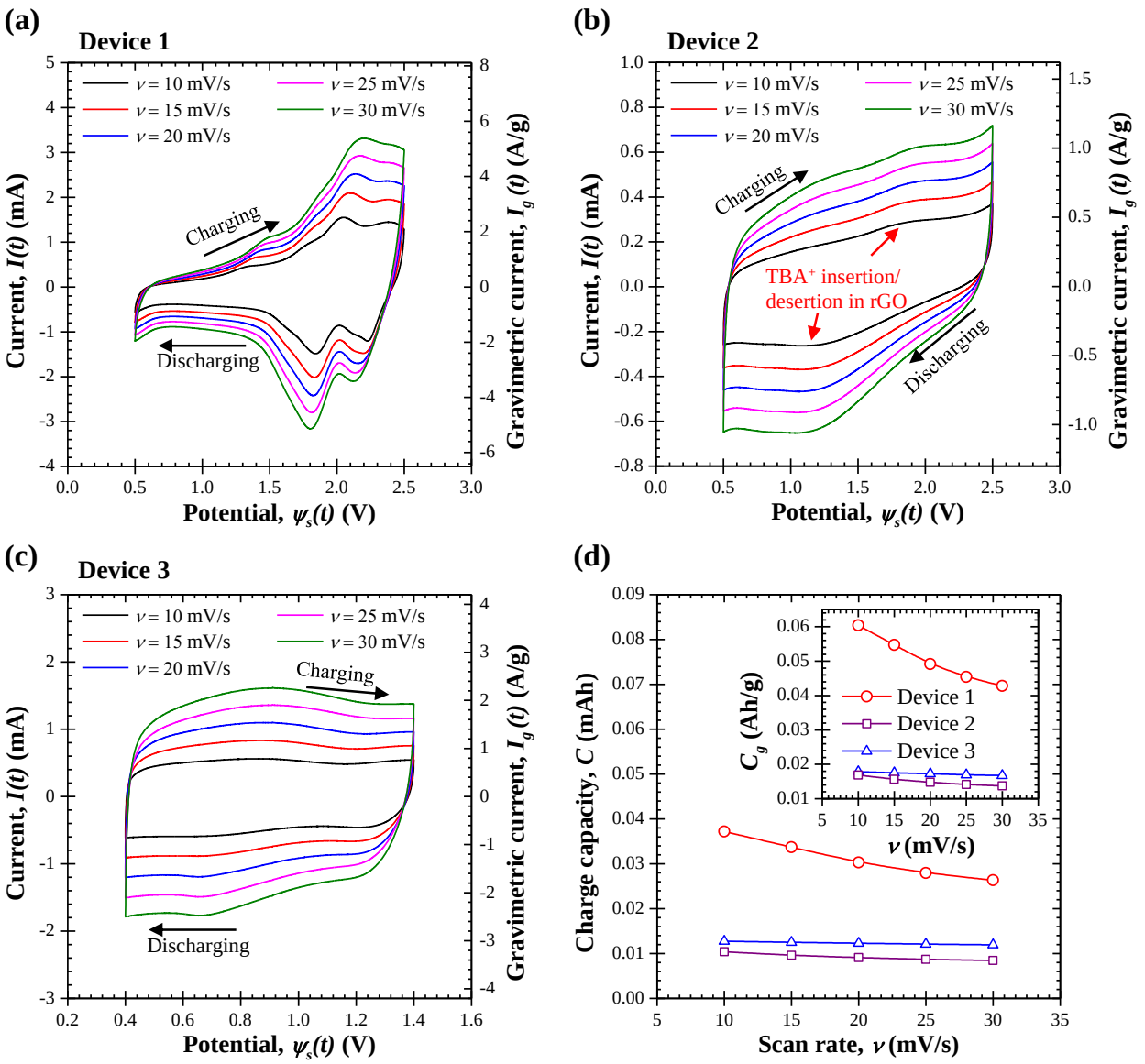

Figure 2: CV curves for (a) Device 1 and (b) Device 2 both with potential window between $\psi_{s,min} = 0.5$ V and $\psi_{s,max} = 2.5$ V and (c) Device 3 with potential window between $\psi_{s,min} = 0.4$ V and $\psi_{s,max} = 1.4$ V for scan rate $\nu = 10$, 15, 20, 25, and 30 mV/s. (d) Charge capacity C for Devices 1, 2, and 3 as a function of scan rate ν ranging from 10 to 30 mV/s.

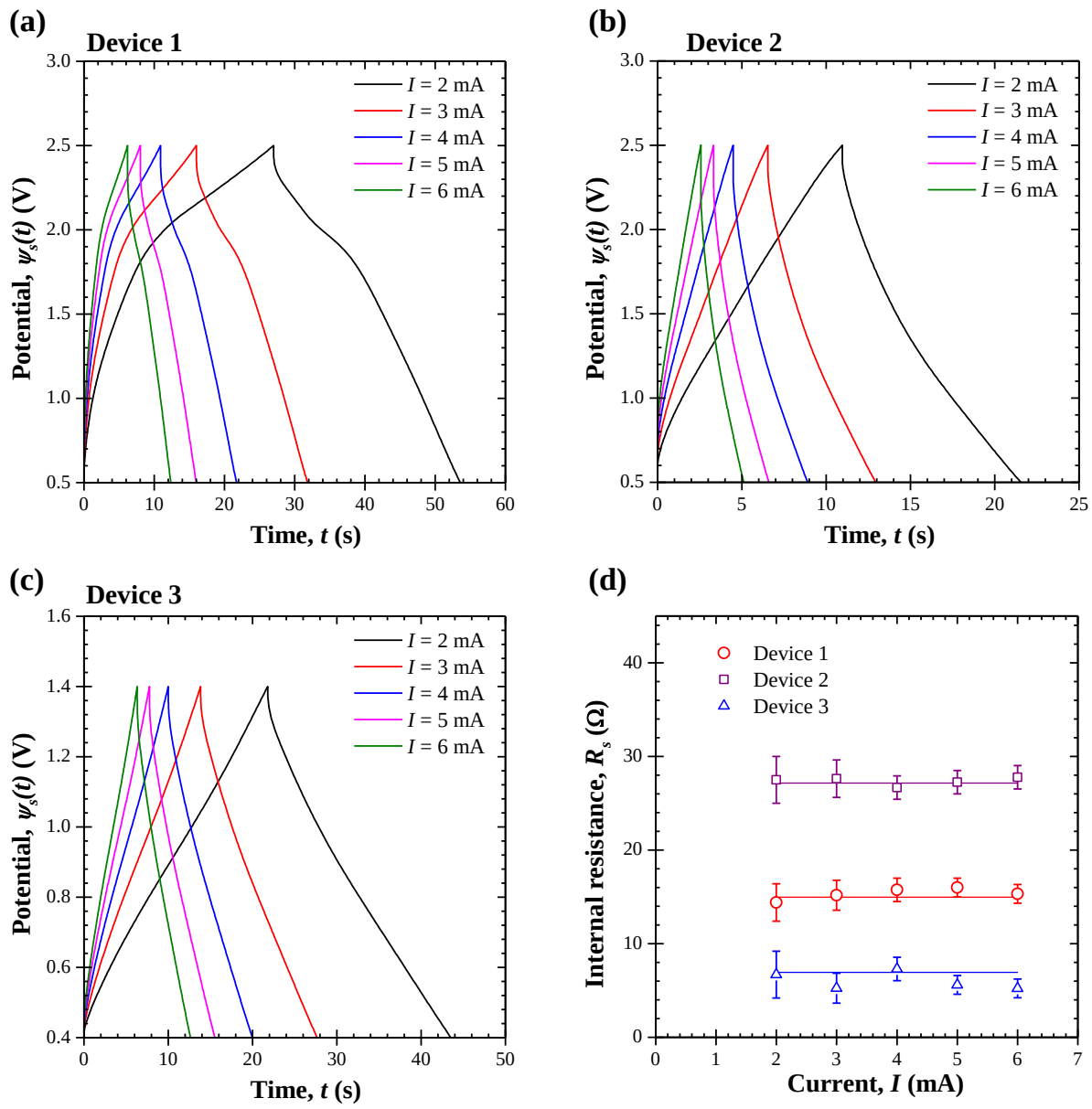

Figure 3: Cell potential evolution during galvanostatic cycling for (a) Device 1, (b) Device 2, and (c) Device 3 under constant current I between 2 and 6 mA. (d) Internal resistance $R_s(I)$ estimated from Equation (7) for Devices 1, 2, and 3 as a function of imposed current I.

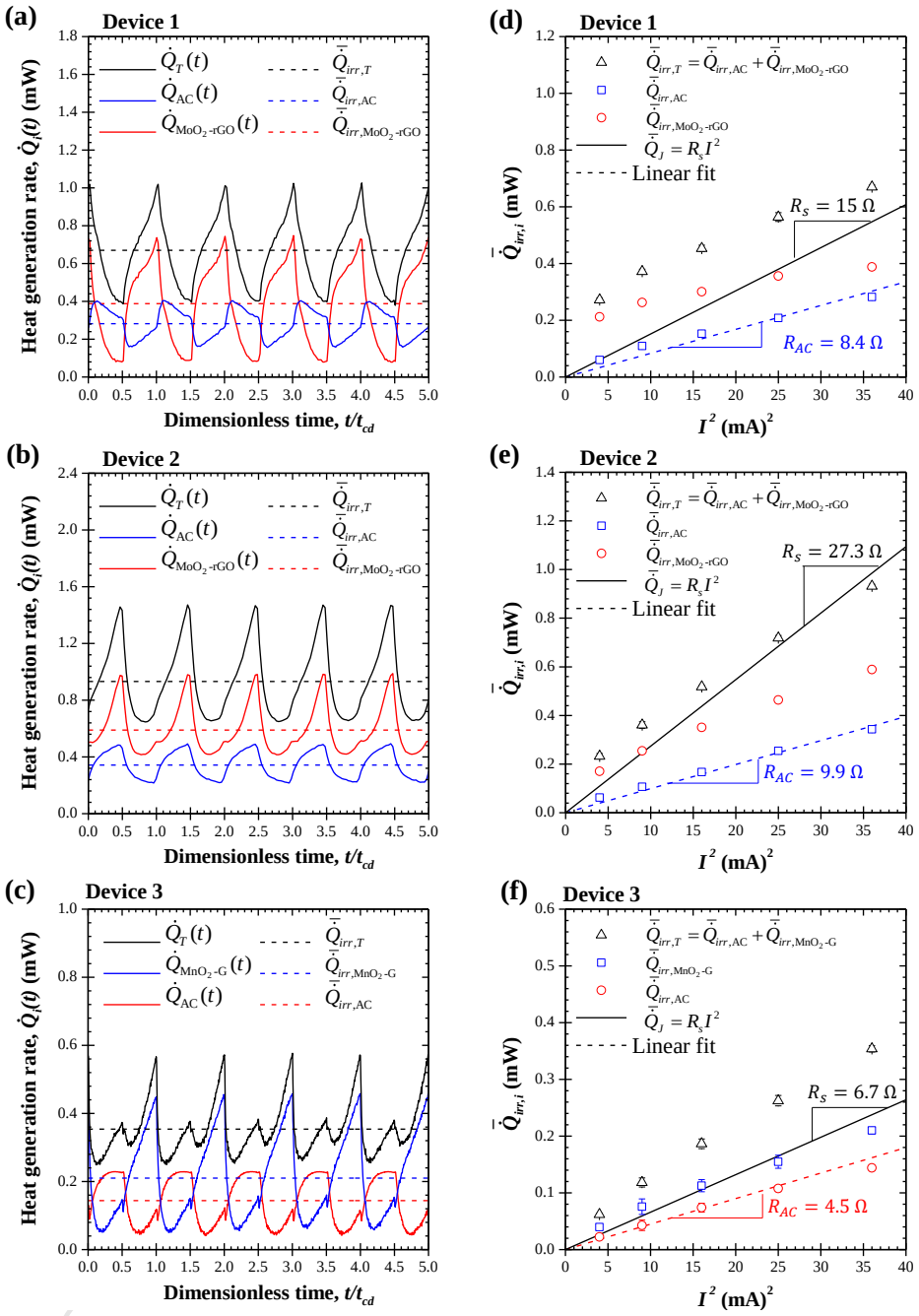

Figure 4: Time-dependent heat generation rates $\dot{Q}_i(t)$ at individual electrodes of (a) Device 1, (b) Device 2, and (c) Device 3 as functions of dimensionless time t/t_{cd} under constant current $I = 6$ mA. Corresponding time-averaged heat generation rate $\bar{\dot{Q}}_{irr,i}$ at individual electrodes for (d) Device 1, (e) Device 2, and (f) Device 3 under galvanostatic cycling as functions of I^2 for current I ranging between 2 and 6 mA.

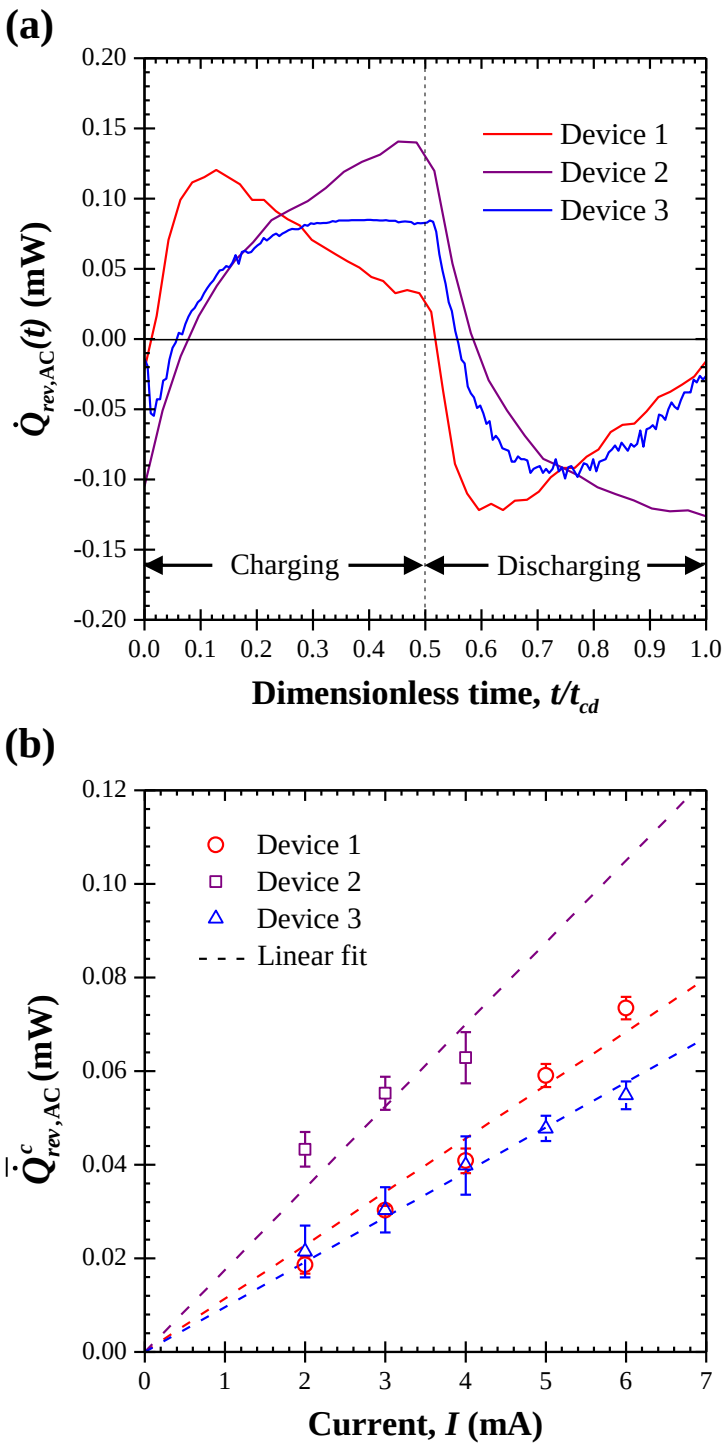

Figure 5: (a) Instantaneous reversible heat generation rate $\dot{Q}_{rev,\mathrm{AC}}(t)$ [Equation (10)] as a function of dimensionless time t/t_{cd} for Devices 1, 2, and 3 for constant current $I = 6$ mA. (b) Time-averaged reversible heat generation rate $\bar{\dot{Q}}^{c}_{rev,\mathrm{AC}}$ [Equation (11)] during the charging step at AC electrode as a function of current I for Devices 1, 2, and 3.

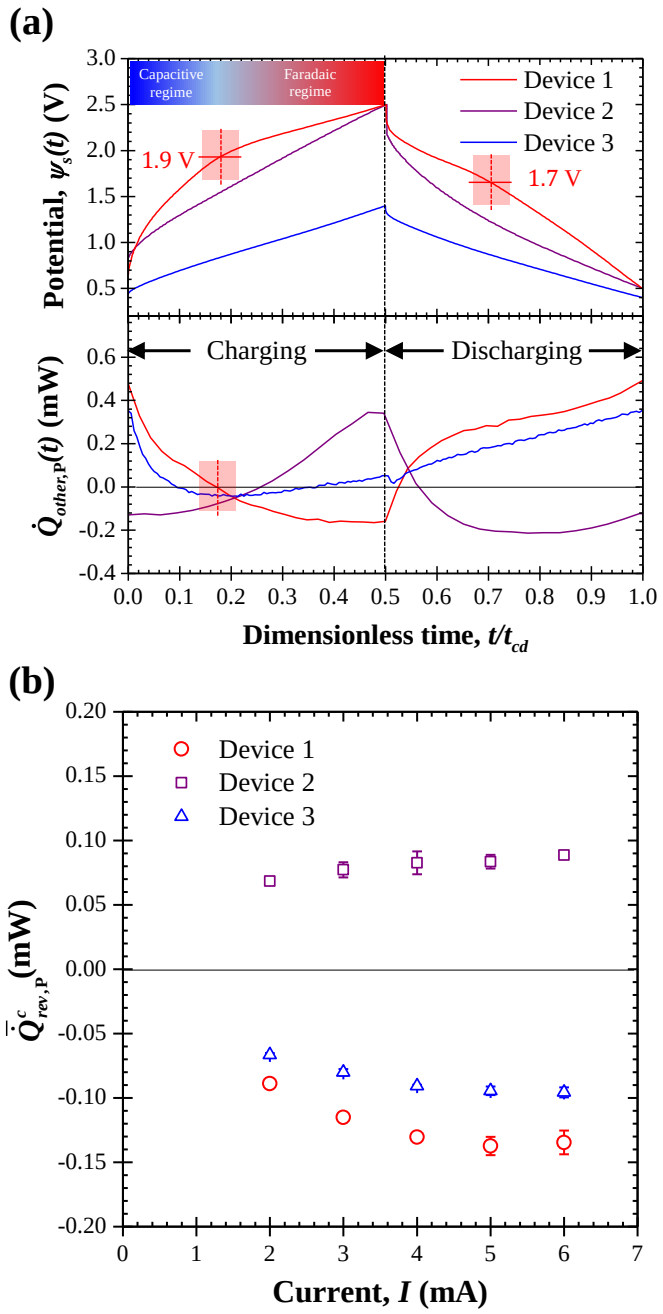

Figure 6: (a) Instantaneous heat generation rate $\dot{Q}_{other,\mathrm{P}}(t) = \dot{Q}_{\mathrm{P}}(t) - \dot{Q}_{J,\mathrm{P}}(t)$ and the corresponding potential evolution $\psi_s(t)$ at the pseudocapacitive electrodes of Devices 1, 2, and 3 as a function of dimensionless time t/t_{cd} for current $I = 6$ mA. (b) Time-averaged reversible heat generation rate during the charging step $\bar{\dot{Q}}^{c}_{rev,\mathrm{P}}$ [Equation (14)] at the pseudocapacitive electrodes as a function of current I for Devices 1, 2, and 3.